JOURNAL OF MATERIALS SCIENCE 25 (1990) 1529–1536

Microstructural characteristics in Ni/zirconia bonding

J. G. DUH, W. S. CHIEN
Department of Materials Science and Engineering, National Tsing Hua University, Hsinchu, Taiwan

Zirconia with various dopants of Y_2O_3 and CeO_2 was employed in the solid state bonding of an Ni/ceramic assembly. The interfacial microstructure of the bonding assembly was examined by electron microscopy and X-ray diffraction and the bonding strength was evaluated with a tensile test under constant pressure. An intermediate layer was observed in the interface of the $3Y_2O_3$–$10CeO_2$–ZrO_2/Ni bonding assembly which revealed that the solid state bonding of Ni/zirconia required the formation of a thin oxide layer to wet the ceramics. In the Ni/zirconia bonding, the growth of NiO was influenced by the dopants in the zirconia. This would, in turn, result in different bonding strengths between ZrO_2 and nickel. The highest bonding strength occurred in the $12CeO_2$–ZrO_2/Ni assembly.

1. Introduction

Composite materials are rapidly increasing in importance in modern technology. The nature of the metal/ceramic interfaces is a critical factor in determining the stability and mechanical properties of the composite. There has been great interest in the bonding of ceramics to metals. The application of ceramic-to-metal bonding is widely used in diesel engines, turbochargers [1], dental restoration [2], sensors [3, 4] and vacuum systems [5–8]. Many bonding methods have been reported [9, 10]. Among these, solid-state bonding is achieved by interposing a metallic layer between two ceramics or a metal and a ceramic. The bonding process depends on possible chemical interactions between the metal and the ceramic and also on contact growth [11]. For a noble metal/ceramic system, extensive reaction and migration of the metallic phase from the bond area were observed in the Pt–Al_2O_3 system [12]. Platinum reacted strongly with Al_2O_3, ZrO_2 and ThO_2 under conditions of low oxidizing potential [13, 14]. For a non-noble metal/ceramic system, the bonding strength depends on bonding pressures, times, temperatures and atmosphere, and a diffuse layer of compositional variations is produced. In some studies [5, 15], the bonding strength increased with the increasing bonding time and pressure. Nevertheless, Yamane *et al.* [16] reported a maximum shear strength obtained for 15 min bonding in air for PSZ/Ni at 1173 K.

In this study, bonding assemblies between nickel and zirconia-based ceramics were employed to investigate the interfacial phenomenon in solid state bonding. Nickel is considered to be a model metal and zirconia has attracted much attention in wide ranges of application. The morphological development of Ni/zirconia bonding is evaluated by electron microscopy. The bonding strength in the metal–ceramic joint is investigated as a function of firing at constant load. The interrelation in the bonding assembly and the measured strength will be discussed.

2. Experimental procedure

Three types of zirconia ceramics were employed in the ceramic/metal bonding system. 3 mol % yttria-stabilized zirconia (YSZ3, Toyo Soda Co., Tokyo, Japan) was chosen for its high fracture toughness, which is unaffected by thermal cycling [17]. 12 mol % CeO_2–ZrO_2 was used because of its high fracture toughness, and resistance to phase transformation during the low-temperature ageing [18]. A third composition with 3 mol % Y_2O_3–10 mol % CeO_2–ZrO_2 was also employed. The ceria-containing zirconia was fabricated using a coprecipitation method [19, 20]. The samples of zirconia were prepared by sintering at 1773 K for 1.6 h.

Pure nickel foil, 0.05 mm thick, was employed to bond with zirconia. For the bonding test, the zirconia

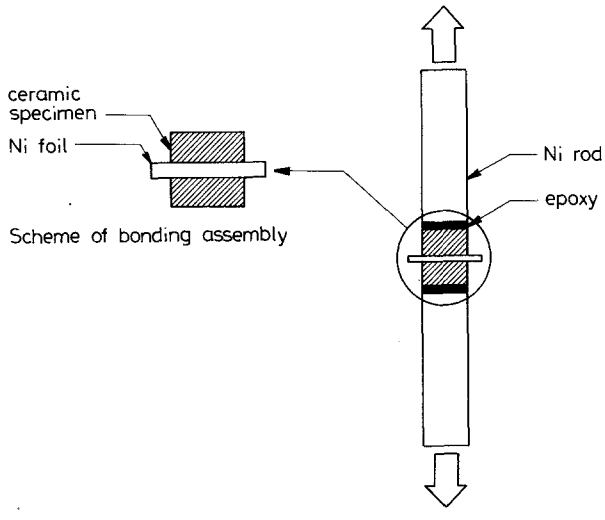

Figure 1 Specimen assembly for tensile measurement.

0022–2461/90 $03.00 + .12 © *1990 Chapman and Hall Ltd.*

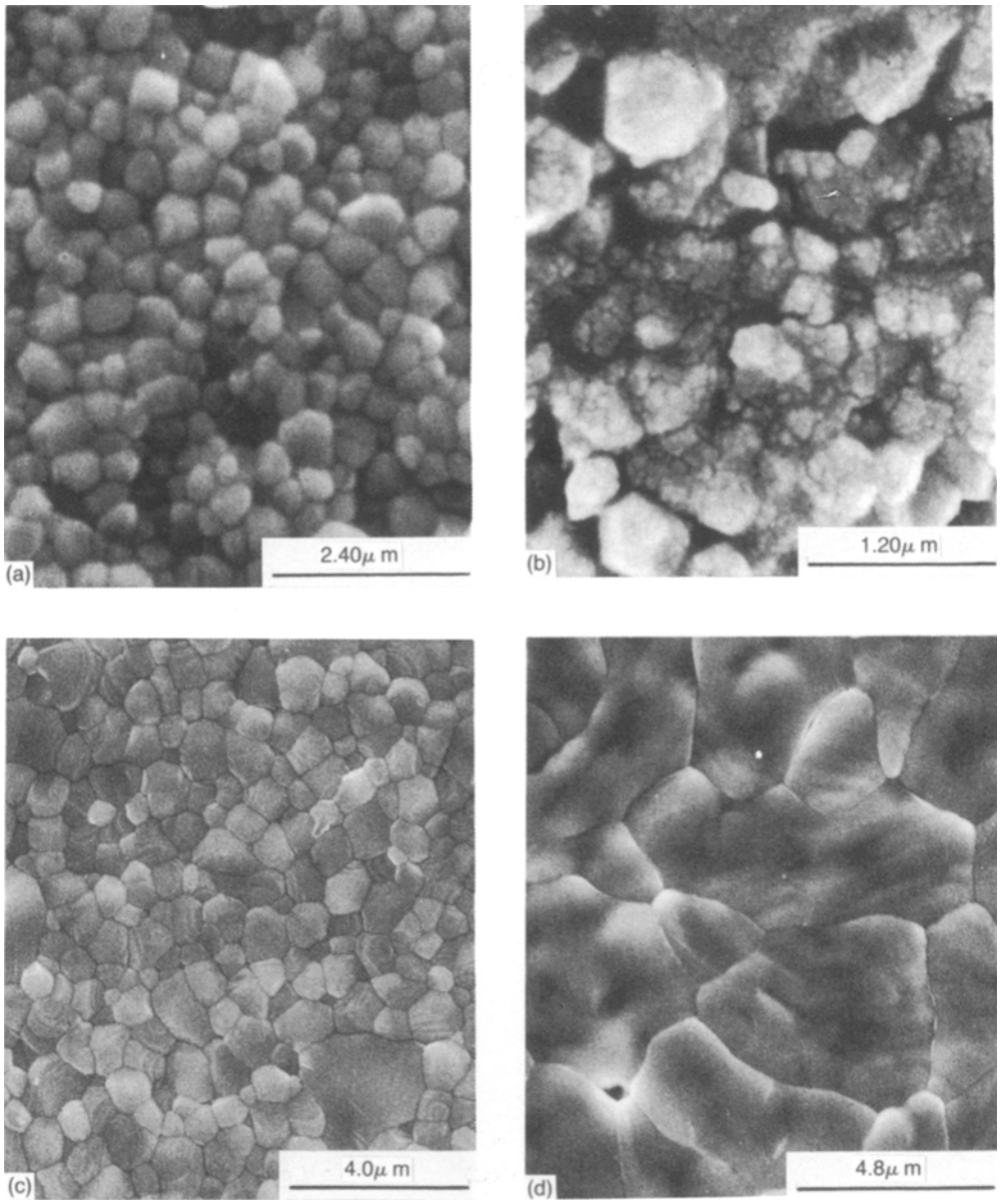

Figure 2 Scanning electron micrographs of ZrO_2-based ceramics: (a) as-sintered surface of YSZ3; (b) fracture surface of YSZ3; (c) as-sintered surface of $3Y_2O_3$–$10CeO_2$–ZrO_2; (d) as-sintered surface of $12CeO_2$–ZrO_2.

pellets were polished to optical flatness on one end with 1 to 6 μm diamond paste as the final abrasive. The metal and zirconia samples were cleaned before use by ultrasonic agitation in acetone.

The Ni/zirconia assembly was fired at constant pressure, and the heating rate for the bonding apparatus was estimated to be 30 K min^{-1} below 1273 K. The bonding strength was measured by a tensile test, as indicated in Fig. 1. The ratio of contact area was measured from the micrograph of the fracture surface of the Ni/zirconia sample.

The microstructural development in the metal/ceramic bonding was examined with a computer-automated electron microprobe (Jeol JCXA-733, Tokyo, Japan) and a transmission electron microscope (TEM, Jeol 100CX). In addition, an X-ray diffractometer was employed for phase identification.

3. Results and discussion

In order to investigate the effect of the dopant on the bonding strength of the ZrO_2–Ni assembly, various dopants, including Y_2O_3 and CeO_2 were employed in ZrO_2 ceramics. Fig. 2 shows the scanning electron micrographs of the ZrO_2-based ceramics. It is apparent that ceria-containing zirconia exhibits larger grain growth.

TABLE I Grain size, crystalline size and phase of various zirconia

	YSZ3	$3Y_2O_3$–$10CeO_2$–ZrO_2	$12CeO_2$–ZrO_2	Pure ZrO_2
Phase	c + t	c + t	t + m	m
Grain size (μm)	0.38	0.67	2.4	2.04
Crystalline size (nm)	36.9 (t)	39.2 (t)	42.8 (t) 43.5 (m)	42.6 (m)

t, tetragonal; c, cubic; m. monoclinic.

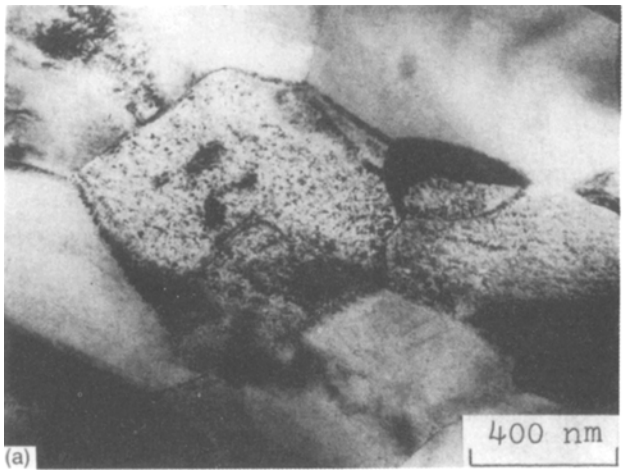

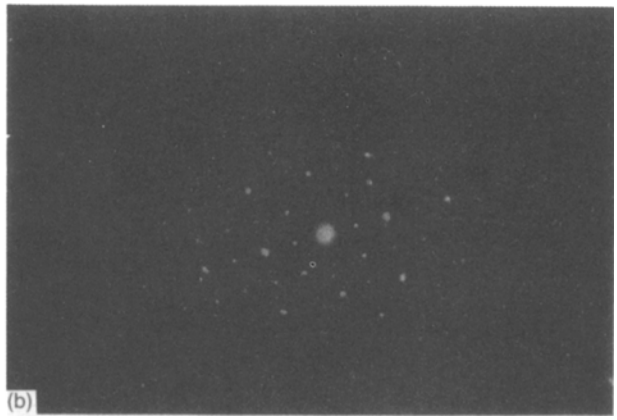

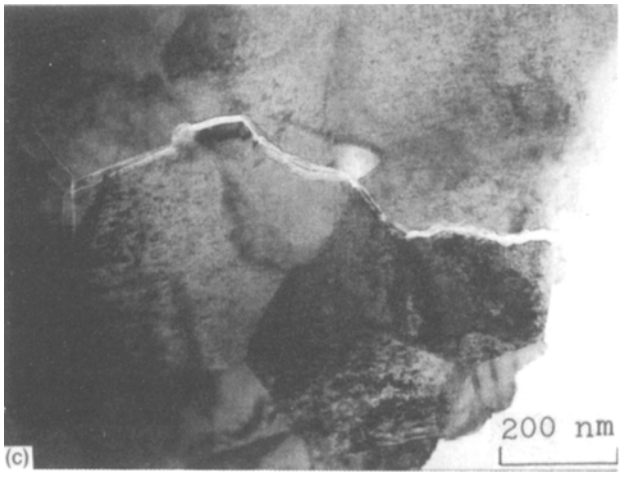

Figure 3 (a) The bright-field image of YSZ3; (b) corresponding $[1\,0\,0]_c$ selected-area diffraction pattern. (c) The bright-field image of YSZ3; a crack is visible.

The phase, grain size and crystalline size are listed in Table I. The crystalline size, D, is calculated using the Scherrer formula [21]

$$D = 0.9\lambda(\beta \cos \theta) \quad (1)$$

where λ is the X-ray wavelength, β is the corrected half-width and θ is the Bragg's angle.

Fig. 3a and b show the TEM bright-field image of YSZ3 and corresponding $[1\,0\,0]_c$ selected-area diffraction pattern. A crack is visible in Fig. 3c, which indicates that the propagation of the crack is transgranular. Fig. 4 presents the TEM bright-field image of a grain, g, in the specimen $12CeO_2$–ZrO_2, and the corresponding $[1\,1\,1]_0$ and $[1\,0\,0]_0$ selected-area diffraction patterns. Fig. 5 shows the TEM bright-field image of another grain, A, in $12CeO_2$–ZrO_2, and the corresponding $[1\,1\,1]_m$ selected-area diffraction pattern. The grain sizes of grains g and A are about 1.7 and 2.8 μm, respectively. According to Tsukuma's study [18], the critical grain size of the retention of the tetragonal phase for $12CeO_2$–ZrO_2 was about 2.8 μm. As a result, the 1.7 μm grain size can retain the tetragonal phase. However, as the grain size is larger than 2.8 μm, the tetragonal phase cannot be retained and the monoclinic phase is produced. Fig. 6 shows the transmission electron micrograph and corresponding selected-area diffraction pattern of $3Y_2O_3$–$10CeO_2$–ZrO_2. The wave-like morphology is probably attributed to the ion milling in the sample preparation.

Fig. 7 represents the (electron spectroscopy for chemical analysis (ESCA)) spectra of the fracture

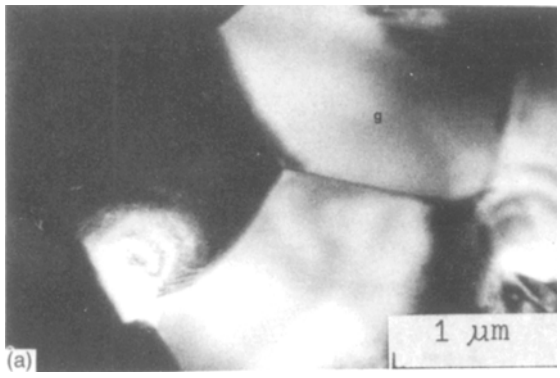

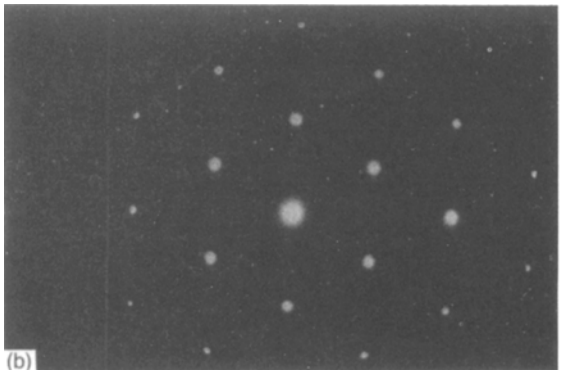

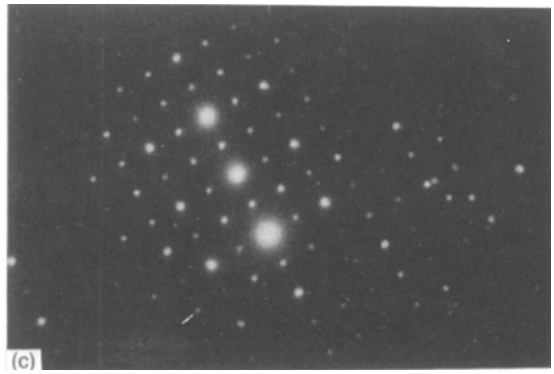

Figure 4 (a) The bright-field image of $12CeO_2$–ZrO_2. (b) $[1\,1\,1]_0$ selected-area diffraction pattern of grain g. (c) $[1\,0\,0]_0$ selected-area diffraction pattern of grain g.

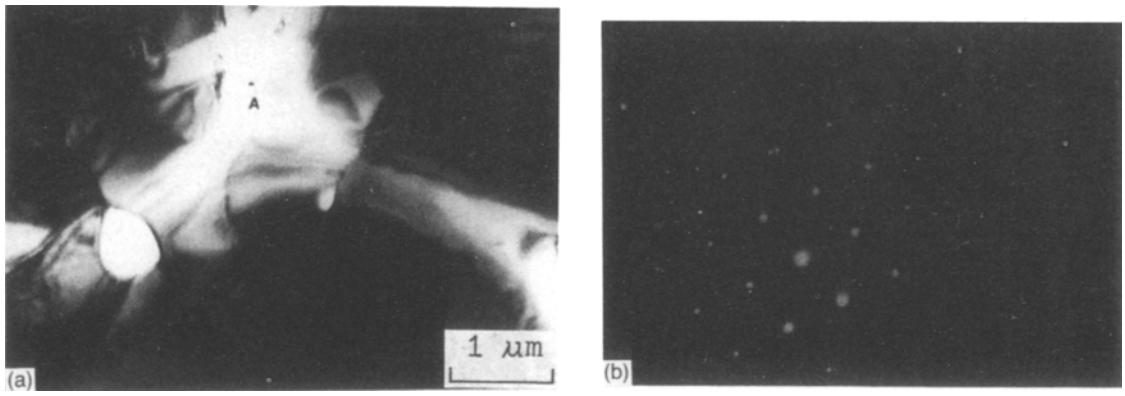

Figure 5 (a) The bright-field image of $12CeO_2$–ZrO_2. (b) $[1\,1\,1]_m$ selected-area diffraction pattern of grain A.

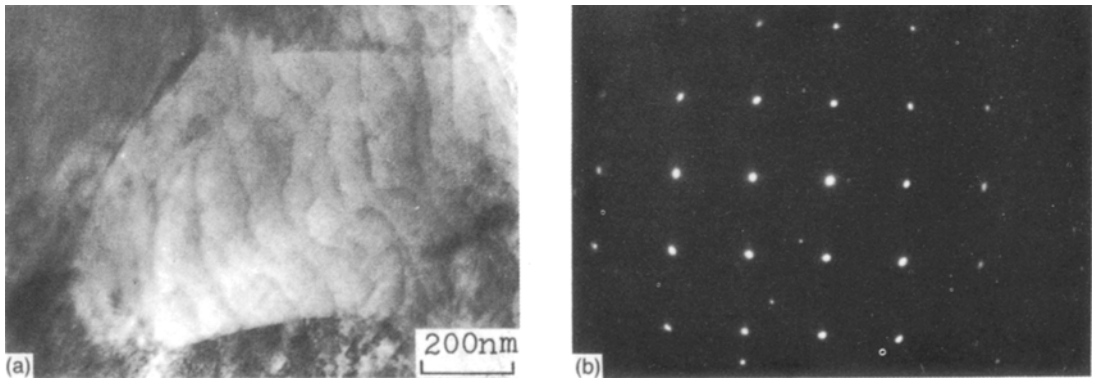

Figure 6 (a) The bright-field image of $3Y_2O_3$–$10CeO_2$–ZrO_2, (b) corresponding $[0\,0\,1]_t$ selected-area diffraction pattern.

surface in YSZ3–Ni. The oxidation states of zirconium and nickel are evaluated to be ZrO_2 and NiO, respectively, from the spectra. The X-ray diffraction pattern of the fracture surface in YSZ3–Ni is shown in Fig. 8, in which the peaks are identified as ZrO_2 (c, t) and NiO. On the basis of Figs 7 and 8, it is found that no intermediate compound is formed between nickel and zirconium when nickel is bonded to ZrO_2 in air.

Fig. 9 shows a scanning electron micrograph of the cross-sectional view in an Ni–ZrO_2 assembly bonded at 900° C for 2 h in air. The assembly is of a sandwich type YSZ3/Ni/$3Y_2O_3$–$10CeO_2$–ZrO_2. The interface appears to be continuous and no large voids are observed. This is in agreement with the results reported by Rhines and Connel [22], and Sawhill and Hobbs [23], in which there is no vacancy accumulating at the Ni/NiO interface when new oxide grows.

Fig. 10 shows the scanning electron micrograph, line profiles and X-ray mapping of nickel, zirconium and cerium in the vicinity of the bonding interface for $3Y_2O_3$–$10CeO_2$–ZrO_2/Ni specimen bonded at 900° C for 2 h in air. According to the profile of zirconium, cerium and nickel, it is apparent that there is an intermediate layer between nickel and $3Y_2O_3$–$10CeO_2$–ZrO_2, which is believed to be NiO based on the X-ray diffraction, as shown in Fig. 8. A similar result is observed in the YSZ3/Ni assembly at 900° C for 2 h in air. However, the layer thickness between Ni and YSZ3 is smaller than that in $3Y_2O_3$–$10CeO_2$–ZrO_2/Ni. It should be pointed out that nickel could not be bonded to YSZ3 when bonded in vacuum. This implies that the bonding of YSZ3/Ni requires the formation of a thin oxide layer to wet the YSZ3 ceramic.

Bonding between various doped ZrO_2 and nickel is employed to study the influence of the degree of bonding in the interfacial bonding strength, which is represented by the ratio P_H defined as

$$P_H = A_{ap}/A_p \quad (2)$$

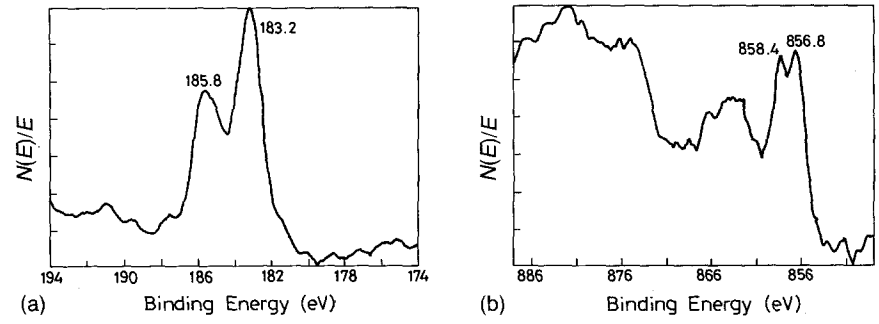

Figure 7 The ESCA spectra of the fracture surface for YSZ3–Ni system.

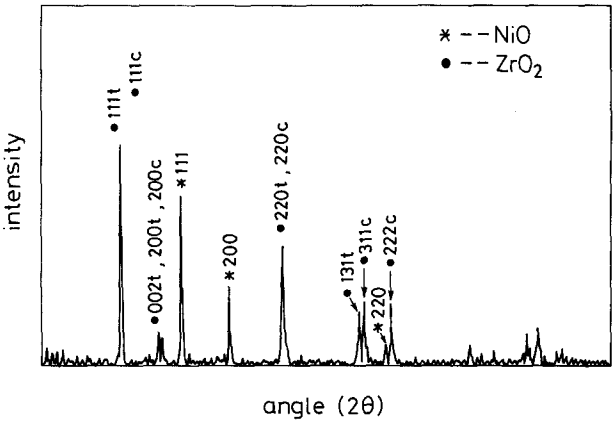

Figure 8 The X-ray diffraction pattern of the fracture surface for the solid–solid state bonding of YSZ3–Ni.

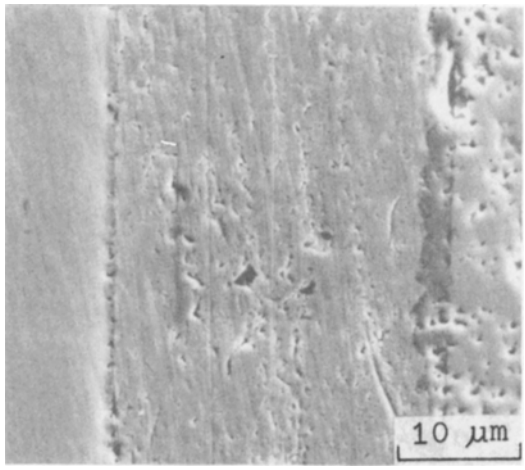

Figure 9 A scanning electron micrograph of the cross-section of YSZ3/Ni/$3Y_2O_3$–$10CeO_2$–ZrO_2 assembly bonded for 2 h at 900° C in air.

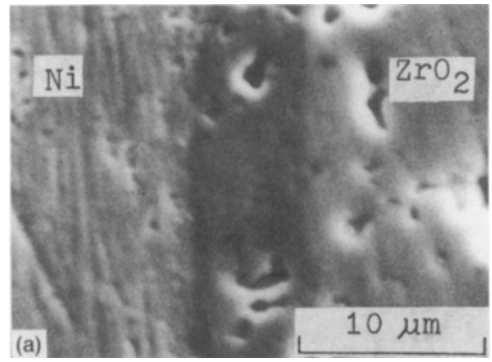

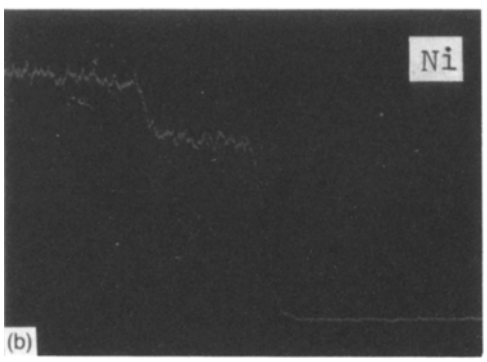

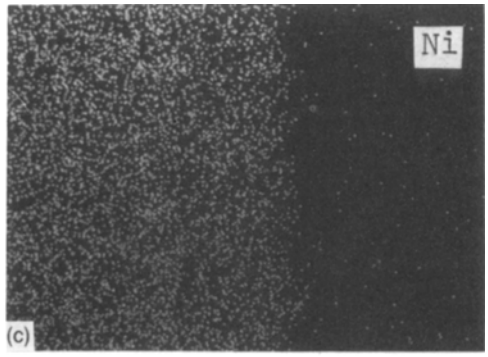

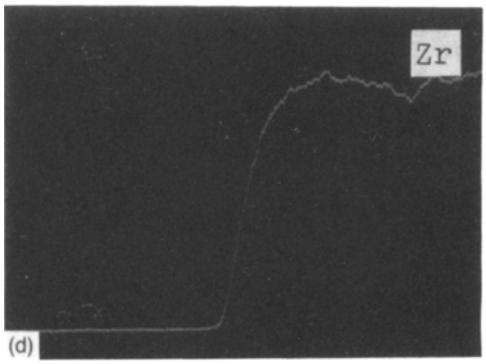

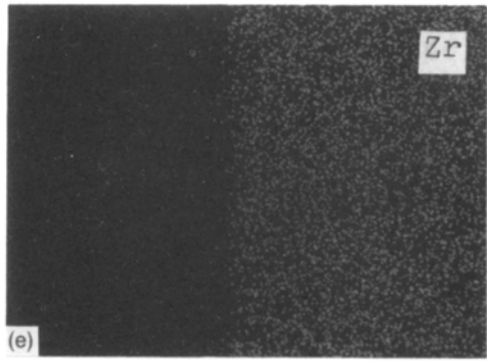

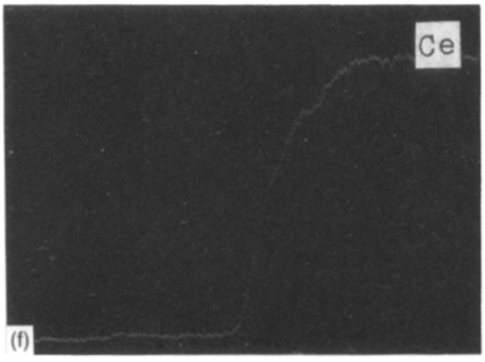

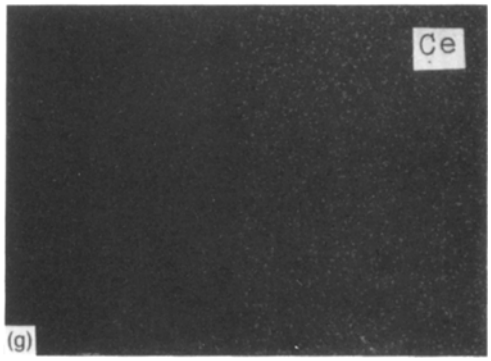

Figure 10 EPMA result in $3Y_2O_3$–$10CeO_2$–ZrO_2/Ni system: (a) SEM, (b) nickel line profile, (c) nickel X-ray mapping, (d) zirconium line profile (e) zirconium X-ray mapping, (f) cerium line profile, (g) cerium X-ray mapping.

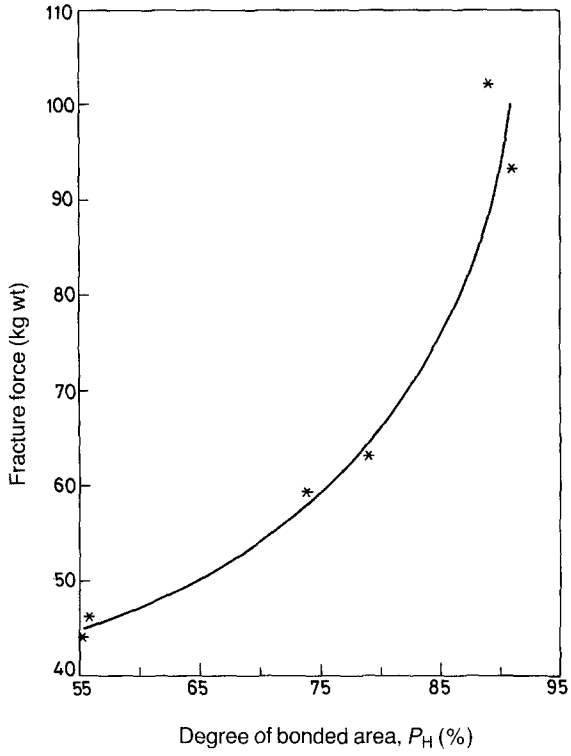

Figure 11 The fracture force as the function of the degree of the bonded area for $12CeO_2$–ZrO_2/Ni bonded for 2 h at 900° C in air.

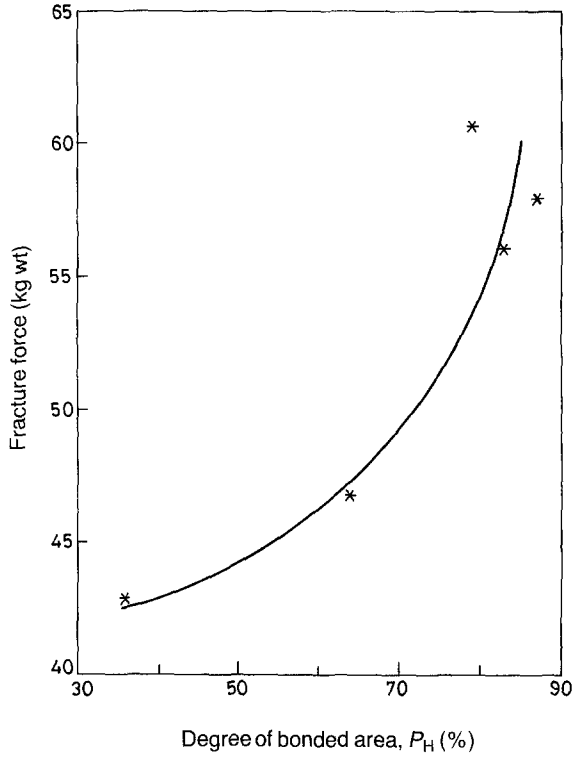

Figure 13 The fracture force of the degree of the bonded area for YSZ3/Ni bonded for 2 h at 900° C in air.

where A_{ap} is the bonded interfacial area and A_p the total interfacial area. The degree of bonding can be measured at the ceramic–metal interface from the optical micrograph. Figs 11 to 13 clearly indicate that the fracture force increases with increasing bonded area.

Table II lists the bonding strength of various doped ZrO_2–Ni assemblies bonded for 2 h at 900° C in air.

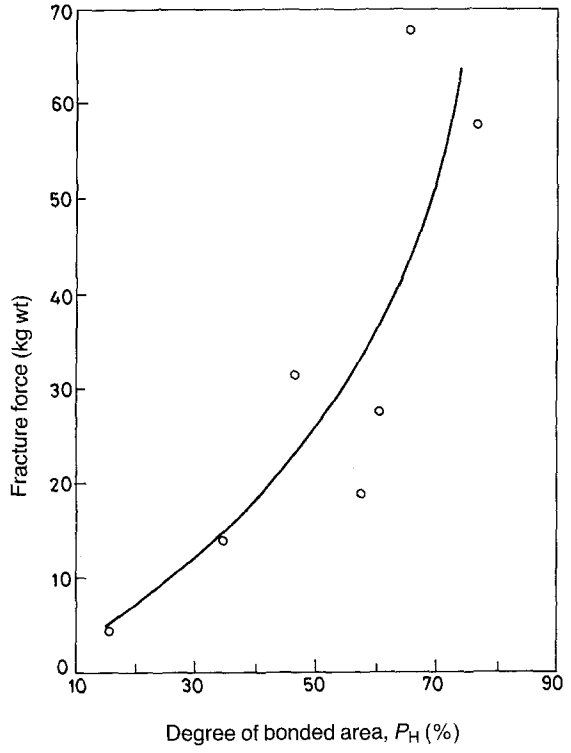

Figure 12 The fracture force as the function of the degree of the bonded area for $3Y_2O_3$–$10CeO_2$–ZrO_2/Ni bonded for 2 h at 900° C in air.

The bonding of $12CeO_2$–ZrO_2/Ni is the strongest, while $3Y_2O_3$–$10CeO_2$–ZrO_2/Ni is the weakest.

In order to study the effect of the bonding time on the strength, a series of bonding tests was carried out for times ranging 0.5 to 3 h under a constant pressure. It seems that the bonding strength increases promptly as the bonding time increases from 0.5 to 1 h, but remains almost unchanged with time up to 3 h, as shown in Fig. 14. It is argued that the NiO adhesion to nickel is a predominant factor for YSZ3–Ni bonding, because all test specimens fractured at the Ni/NiO interface for the YSZ3–Ni assembly. Thus, the mechanism of NiO oxide growth is a decisive

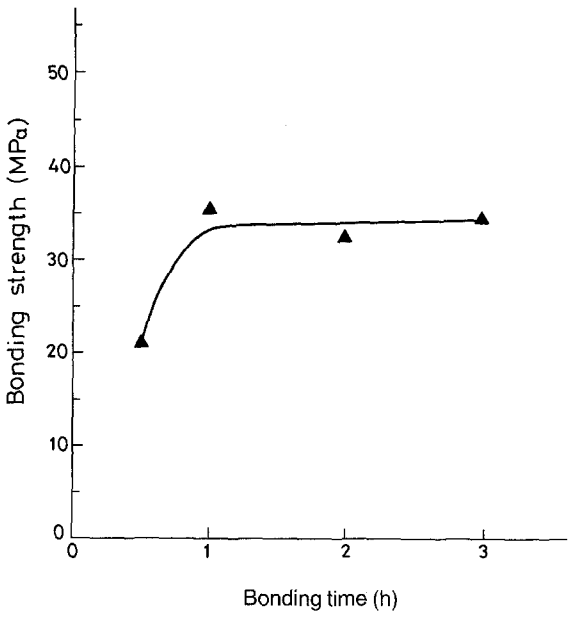

Figure 14 The bonding time dependence of the bonding strength for the YSZ3/Ni system.

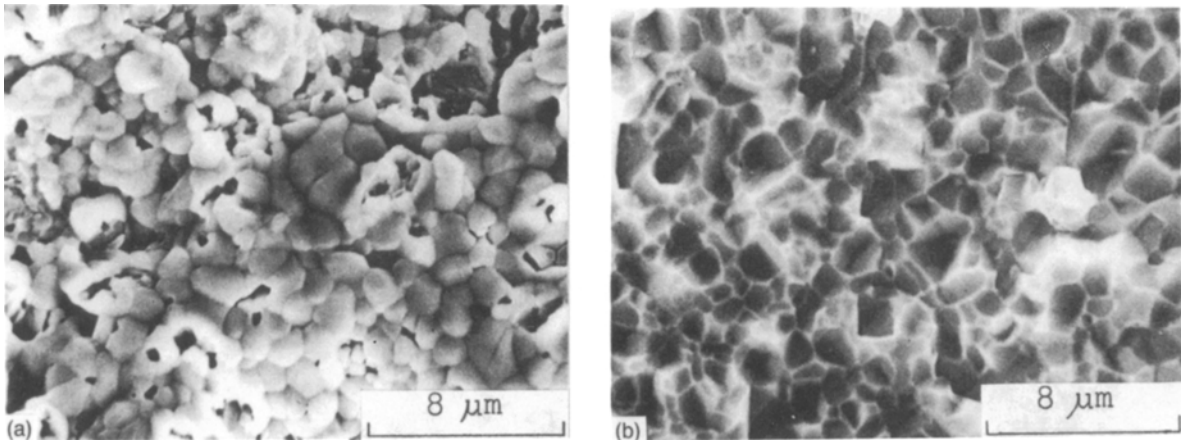

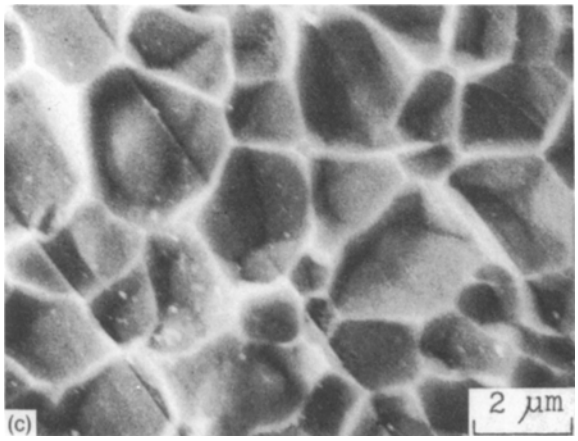

Figure 15 Scanning electron micrograph of the fracture surface for strong YSZ3/Ni bonding: (a) NiO side, (b), (c) nickel side.

factor to the bonding strength for this system. Fig. 15 shows a scanning electron micrograph of the fracture surface in YSZ3–Ni with strong bonding strength, while Fig. 16 shows scanning electron micrographs of the fracture surface in YSZ3–Ni of which the bonding is weak. The weak bonding strength means that the bonding strength is less than 5 MPa. As shown in Figs 15 and 16, the morphology is extremely different on the nickel side. For strong YSZ3–Ni bonding, the dimple-like morphology appears on the nickel side of the fracture surface. However, in weak bonding, the incomplete growth of NiO oxide is observed. As the new NiO oxide grows uniformly throughout the volume of the scale, there is no vacancy accumulation at the Ni/NiO interface when the NiO oxide grows [22, 24]. If the oxide grows completely over the nickel, the bonding strength does not vary with increasing bonding time. The grain size of NiO in the fracture surface for various bonding times is given in Table III. It is observed that the grain size of NiO increases as the bonding time increases.

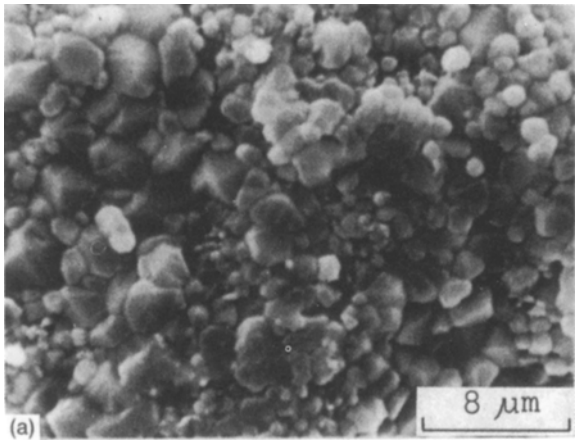

4. Conclusions

1. Solid state bonding between zirconia and nickel was investigated under constant pressure. Three types of zirconia were selected, including 3 mol % yttria-stabilized ZrO_2, 12 mol % CeO_2–ZrO_2 and 3 mol % Y_2O_3–10 mol % CeO_2–ZrO_2.

2. The bonding strength in the YSZ3/Ni assembly increased rapidly with bonding time from 0.5 to 1 h at 900° C, and then reached a saturated value.

Figure 16 Scanning electron micrograph of the fracture surface for weak YSZ3/Ni bonding: (a) NiO side, (b), (c) nickel side.

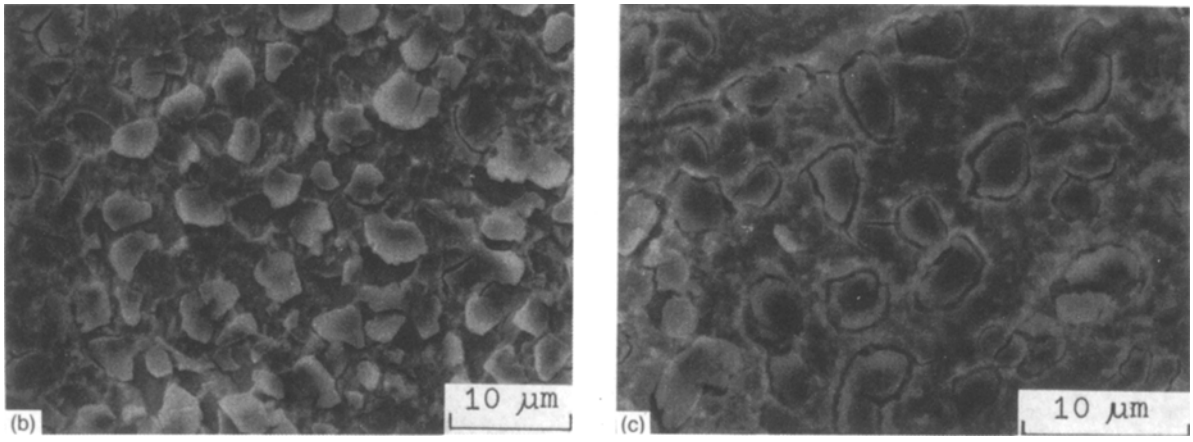

TABLE II The bonding strength between various doped zirconia and nickel

Zirconia	No. of specimens tested	Average bonding strength (MPa)
YSZ3	6	30.6
$3Y_2O_3$–$10CeO_2$–ZrO_2	7	22.6
$12CeO_2$–ZrO_2	6	36.6

3. An intermediate layer of NiO was formed in the interface of $3Y_2O_3$–$10CeO_2$–ZrO_2/Ni bonding at 900° C for 2 h. A similar result was observed in the YSZ3/Ni assembly. Bonding in Ni/zirconia required the formation of a thin oxide layer to wet the ceramics.

4. When the nickel foil was bonded to zirconia, the growth of NiO was affected by the dopants in the zirconia. This, in turn, resulted in different bonding strengths between ZrO_2 and nickel. The $12CeO_2$–ZrO_2/Ni assembly has the highest bonding strength.

5. For strong YSZ3–Ni bonding, a dimple-like morphology appeared on the nickel side of the fracture surface, while an incomplete growth of NiO was observed in the case of weak bonding.

Acknowledgement

The authors thank the National Science Council, Taiwan for financial support under contract no. NSC76-0405-E007-12.

TABLE III The grain size of NiO of the fracture surface for various bonding times

	Bonding time (h)			
	1	2	3	4
Grain size of NiO (μm)	0.62	1.09	1.22	1.58

References

1. M. A. DELUCA, J. W. SWAIN and L. R. SWANK, *Ceram. Engng Sci. Proc.* **8** (1987) 602.
2. A. P. TOMSIA and J. A. PASK, *J. Amer. Ceram. Soc.* **69** [10] (1986) C-239.
3. R. V. ALLEN, W. E. BORBIDGE and P. T. WHELAN, in "Science and Technology of Zirconia II", edited by N. Claussen and A. H. Heuer (American Ceramic Society, Columbus, Ohio, 1981) p. 537.
4. F. P. BAILEY and W. E. BORBIDGE, in "Materials Science Research", Vol. 40, edited by J. Pask and A. Evans (Plenum, New York, 1981) p. 525.
5. H. J. De BRUIN, A. F. MOODIE and C. E. WARBLE, *J. Mater. Sci.* **7** (1972) 909.
6. H. T. De BRUIN, US Pat. 1 352 775.
7. *Idem*, Ital. Pat. 920 003.
8. *Idem*, Brit. Pat. 1 352 775.
9. A. J. KINLOCH, *J. Mater. Sci.* **15** (1980) 2141.
10. H. W. HENNICKE, in "High Tech. Ceramics", edited by P. Vincenzini (Elsevier, Netherlands, 1987) p. 805.
11. M. COURBIERE, D. JUVE and D. TREHEUX, *ibid.*, p. 1053.
12. R. V. ALLEN and W. E. BORBIDGE, in "Science of Ceramics 12" (Ceramurgica, Faenza, Italy) p. 383.
13. A. S. DARLING, G. L. SELMAN and R. RUSHFORTH, *Platinum Met. Rev.* **14** (1970) 54.
14. D. OTT and C. J. RAUB, *ibid.* **20** (1976) 79.
15. S. MOROZUMI, M. KIKUCHI and T. NISHINO, *J. Mater. Sci.* **16** (1981) 2123.
16. T. YAMANE, Y. MINAMINO, K. HIRAO and H. OHMISHI, *J. Mater. Sci.* **21** (1986) 4227.
17. TSK Ceramics Technical Bulletin, Toyo Soda Manufacturing Co. Ltd, No 2–112 (1986).
18. K. TSUKUMA, *Amer. Ceram. Soc. Bull.* **65** (1986) 1386.
19. J. G. DUH, H. T. DAI and W. Y. HSU, *J. Mater. Sci.* **23** (1988) 2786.
20. J. G. DUH, H. T. DAI and B. S. CHIOU, *J. Amer. Ceram. Soc.* **71** (1988) 813.
21. H. K. SCHMID, *ibid.* **70** (1987) 367.
22. F. N. RHINES and R. G. CONNELL Jr, *J. Electrochem. Soc.* **126** (1979) 1061.
23. H. T. SAWHILL and L. W. HOBBS, *J. De Physique, Colloque* **C4** (1985) 117.
24. F. N. RHINES and R. G. CONNELL Jr, *J. Electrochem. Soc.* **124** (1977) 1122.

Received 3 October 1988
and accepted 28 February 1989